

Structural Dynamics of 1,2-Diiodoethane in Cyclohexane Probed by Picosecond X-ray Liquidography

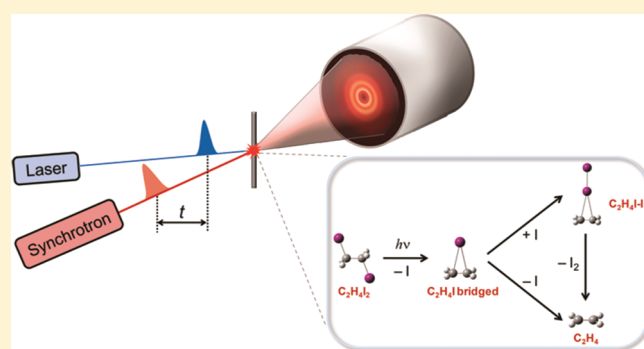
Jeongho Kim,[†] Jae Hyuk Lee,[†] Joonghan Kim,[†] Sunhong Jun,[†] Kyung Hwan Kim,[†] Tae Wu Kim,[†] Michael Wulff,[‡] and Hyotcherl Ihee^{*,†}

[†]Center for Time-Resolved Diffraction, Department of Chemistry, Graduate School of Nanoscience and Technology (WCU), KAIST, Daejeon, Republic of Korea

[‡]European Synchrotron Radiation Facility, Grenoble Cedex 38043, BP 220, France

 Supporting Information

ABSTRACT: We investigate the structural dynamics of iodine elimination reaction of 1,2-diiodoethane ($C_2H_4I_2$) in cyclohexane by applying time-resolved X-ray liquidography (TRXL). The TRXL technique combines structural sensitivity of X-ray diffraction and 100 ps time resolution of X-ray pulses from synchrotron and allows direct probing of transient structure of reacting molecules. From the analysis of time-dependent X-ray solution scattering patterns using global fitting based on DFT calculation and MD simulation, we elucidate the kinetics and structure of transient intermediates resulting from photodissociation of $C_2H_4I_2$. In particular, the effect of solvent on the reaction kinetics and pathways is examined by comparison with an earlier TRXL study on the same reaction in methanol. In cyclohexane, the C_2H_4I radical intermediate undergoes two branched reaction pathways, formation of C_2H_4I-I isomer and direct dissociation into C_2H_4 and I, while only isomer formation occurs in methanol. Also, the C_2H_4I-I isomer has a shorter lifetime in cyclohexane by an order of magnitude than in methanol. The difference in the reaction dynamics in the two solvents is accounted for by the difference in solvent polarity. In addition, we determine that the C_2H_4I radical has a bridged structure, not a classical structure, in cyclohexane.



1. INTRODUCTION

Chemical reactions in solution and liquid phases have been of much interest as many industrially important and biologically relevant reactions occur in solution. Time-resolved X-ray liquidography (TRXL), or time-resolved X-ray solution scattering, has emerged as a powerful technique for studying the solution-phase reaction dynamics because it can monitor in real time the structural dynamics of photoinduced phenomena in the solution phase. Traditionally, time-resolved optical spectroscopies such as pump-probe transient absorption and time-resolved Raman techniques have flourished in studying the fast reaction dynamics in condensed media, but they can probe only specific electronic or vibrational transitions of local chromophores and thus lack the sensitivity to the global molecular structure. The limitation of the time-resolved optical spectroscopy can be complemented by using X-ray pulse as probe. Because X-ray is diffracted (or scattered) off all atom-atom pairs and chemical species present in the molecule, direct information on the global molecular structure can be retrieved from the measured X-ray diffraction patterns. By combining the structural sensitivity of X-ray diffraction and superb time resolution (100 ps) of the X-ray pulses generated from third-generation synchrotron, the TRXL provides rather direct information on the transient structures of

reacting molecules, for example, time-dependent change of bond lengths and angles. In recent years, TRXL has been successfully applied to elucidating the structural dynamics of various molecular systems including diatomic molecules, haloalkanes, organometallic complexes, proteins, and nanoparticles in solution phase.¹⁻¹⁶

The major challenge in understanding the solution-phase chemistry arises from the presence of numerous solvent molecules surrounding solutes, leading to the interaction between solute and solvent. The solute-solvent interaction can have a profound effect on the progress of a chemical reaction by changing the landscape of the potential energy surfaces. In particular, the polarity and geometry of the local solvent environment sensitively alters the rates, pathways, and branching ratios of the chemical reaction in solution.¹⁷⁻¹⁹ Therefore, to have a better understanding of the dynamics and mechanism of solution-phase reactions, it is crucial to take into account the complex influence of the solvent.

Special Issue: Femto10: The Madrid Conference on Femtochemistry

Received: August 15, 2011

Revised: November 24, 2011

Published: November 29, 2011

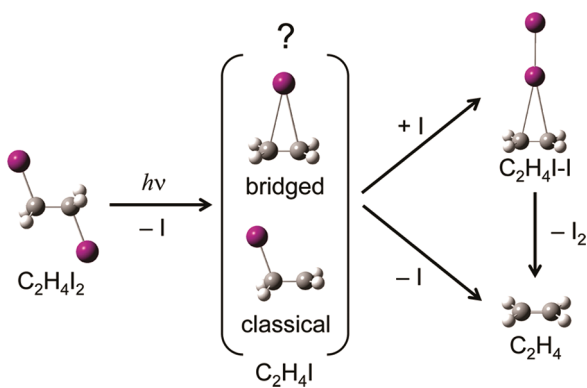


Figure 1. Photoinduced iodine elimination reaction of $C_2H_4I_2$. By photoexcitation, the first iodine is dissociated and C_2H_4I radical is formed. The structure of C_2H_4I radical formed by dissociation of the first iodine atom has been controversial before the earlier work using TRXL revealed that the radical has a bridged structure in methanol. The C_2H_4I radical either reacts with I atom to form C_2H_4I-I isomer (and then dissociates to C_2H_4 and I_2) or directly dissociates into C_2H_4 and I. According to the previous TRXL work of this reaction in methanol solvent, only the former channel (isomer formation) occurs in methanol.

In this work, we explore the solvent effect on photoinduced iodine elimination reaction of 1,2-diiodoethane ($C_2H_4I_2$) in cyclohexane solution by applying the TRXL technique. Photodissociation of haloethane has attracted much interest due to its simple molecular structure and its implication for stereochemistry. In particular, a short-lived haloethyl radical such as CH_2ICH_2 radical formed by dissociation of the first iodine atom plays an important role in determining stereoselectivity of certain chemical processes (see Figure 1).^{20–24} To explain the stereoselectivity observed in free-radical addition reactions, theoretical studies by Skell and co-workers proposed a bridged structure, instead of the classical *anti*-structure, for haloethyl radicals.^{25,26} However, despite many theoretical^{27–30} and experimental efforts,^{31–36} direct structural evidence for the bridged radical structure has been elusive. Especially, many spectroscopic studies made for studying halogen elimination reactions of haloethanes^{34–36} was not able to directly determine the structure of haloethyl radicals due to the lack of structural sensitivity of the spectroscopic tools. Later, the ultrafast electron diffraction (UED) technique, which is sensitive to global molecular structure, was applied to studying photodissociation of $C_2F_4I_2$ in the gas phase, but revealed that C_2F_4I radical is of classical structure, not bridged structure.^{37,38} Only recently, a TRXL study on photodissociation of $C_2H_4I_2$ elucidated that the C_2H_4I radical has the bridged structure in methanol.⁴ This finding demonstrates the power of the TRXL technique in revealing the detailed structure of transient species.

Based on the result of the earlier work on $C_2H_4I_2$ photodissociation in the polar methanol solvent, we here present a study of the same reaction in a nonpolar, aprotic cyclohexane solvent. By analyzing the experimental data using the theoretical analysis protocol combining quantum calculation, molecular dynamics (MD) simulation, and global fitting, we extract the reaction kinetics, mechanism, and conformational structure of the C_2H_4I radical in cyclohexane. Comparison of the results from the TRXL measurements in two solvents of different

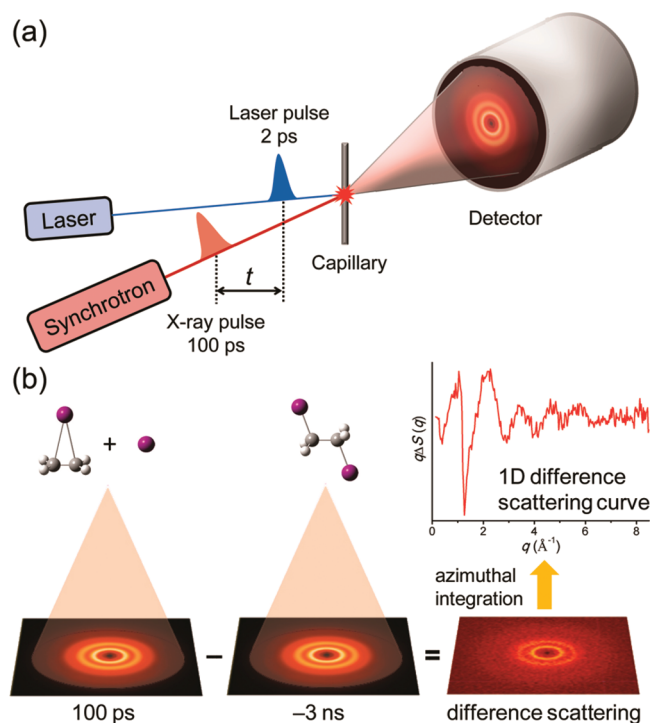


Figure 2. (a) Schematic of the setup for TRXL experiment. The optical laser pulse initiates the photoinduced reaction, and after a well-defined time delay, a X-ray pulse is diffracted off the photoexcited sample. By taking the difference between the diffraction patterns obtained before and after the laser interaction, we can extract the information on the structural change of the reacting molecules. (b) The difference scattering image is obtained by taking the difference between the scattering image measured at a positive time delay (e.g., 100 ps) and the reference scattering image measured at a negative time delay (e.g., -3 ns). The obtained difference scattering image can be reduced to one-dimensional (1D) scattering curve by azimuthally integrating the difference image.

polarities allows us to examine how the solvent influences the reaction dynamics.

2. EXPERIMENTAL SECTION

TRXL is a pump–probe method that employs the laser pulse as pump and the hard X-ray pulse as probe, as shown in Figure 2. A photoreaction of interest is initiated by a laser pulse and the progress of the reaction is monitored by a time-delayed X-ray pulse scattered (or diffracted) off the sample. The obtained time-dependent scattering patterns contain the information on the transient structure of reacting molecules. By analyzing the difference scattering signals measured at various pump–probe time delays, the reaction dynamics can be revealed. For the analysis of experimentally measured data, the experimental curves are globally fit by theoretical scattering curves using a least-squares fitting method. The theoretical scattering curves for all the chemical species potentially involved in the reaction are generated from the molecular structure calculated by high-level DFT calculation and the pair distribution functions, $g(r)$, obtained from MD simulation. More details of the TRXL method are given in our review articles.^{1–3}

Methods and Materials. The TRXL experiments were performed on the beamline ID09B at the European Synchrotron Radiation Facility (ESRF). The detailed setup of the TRXL

experiment is described elsewhere.^{1–3} Briefly, a typical pump–probe scheme consisting of optical pump and X-ray probe pulses was employed to initiate and monitor the chemical reaction, respectively. A laser pulse at 267 nm was generated by frequency-tripling the 800 nm output from an amplified Ti:sapphire laser system and used to trigger the photodissociation reaction of C₂H₄I₂. In order to prevent multiphoton excitation, the laser pulse was temporally stretched to ~2 ps by transmission through a fused silica rod of 30 cm length. The laser pulse of 40 μJ pulse energy was focused to a diameter of 100 μm at the sample, giving a fluence of 4 mJ/mm². Subsequently, a time-delayed X-ray pulse was scattered off the sample to probe the progress of the reaction. The X-ray pulse was ~100 ps long with 5 × 10⁸ photons per pulse and has a quasi-monochromatic spectrum peaked at 18.2 keV with 0.45 keV bandwidth. The X-ray pulse was selected from the 16-bunch filling mode of the synchrotron ring using a synchronized mechanical chopper and focused to a spot of 100 × 85 μm² on the sample. The temporal overlap between X-ray and laser pulses was monitored by a fast GaAs detector, and the time delay was varied electronically with 5 ps precision. The laser and X-ray pulses were also spatially overlapped in a quasi-parallel geometry with a cross-angle of 10°. The two-dimensional (2D) scattering patterns were collected with an area detector (MARCCD, Mar Systems, 2048 × 2048, 64.3 μm effective pixel size) with a sample-to-detector distance of 43 mm and an exposure time of 3 s. The solution sample was prepared by dissolving C₂H₄I₂ (Aldrich, 99.99%) in cyclohexane at 60 mM concentration and was circulated through a capillary of 1 mm thickness. The nozzle provides a stable flow of liquid and allows the refreshment of the liquid sample between subsequent laser pulses at a repetition rate of 1 kHz. The solution scattering signals were measured at various time delays between the laser and X-ray pulses (–100 ps, 100 ps, 300 ps, 1 ns, 3 ns, 10 ns, 30 ns, 70 ns, and 100 ns). In addition, the signal at a negative time delay (–3 ns) was measured as a reference for the unexcited sample and was used for obtaining the difference scattering signal.

Data Processing. The 2D scattering patterns recorded on the CCD detector were azimuthally integrated into 1D intensity curves, $S(q,t)$, as a function of momentum transfer $q = (4\pi/\lambda)\sin(2\theta/2)$, where λ is the wavelength of the X-ray and the 2θ is the scattering angle) and time delay t between the laser and X-ray pulses. The curves were averaged and scaled to the total scattering of one cyclohexane molecule, both elastic and inelastic, from nonexcited solvent/solute background in the high q region, where the scattering is insensitive to structural changes. After scaling the intensities, difference-scattering curves were generated by subtracting the reference data measured at –3 ns from the data at other time delays. Then, q is multiplied to $\Delta S(q,t)$ to magnify the intensities at high scattering angles. The correlated difference radial distribution function (RDF), $r\Delta S(r,t)$, which provides radial electron density change as a function of interatomic distance r in real space, was obtained by sine-Fourier transforming the $q\Delta S(q,t)$ curves:

$$r\Delta S(r,t) = \frac{1}{2\pi^2} \int_0^\infty q\Delta S(q,t) \sin(qr) \exp(-q^2\alpha) dq \quad (1)$$

where the constant α ($\alpha = 0.03 \text{ \AA}^2$) is a damping constant used to account for the finite q range of the experimental data.

Data Analysis. The treated data curves, $q\Delta S(q,t)$, were analyzed using our homemade algorithm for weighted least-squares fitting that minimizes the chi-square (χ^2) difference

between the experimental data and the theoretical model function. Because the experimental $q\Delta S(q,t)$ data at various time delays are related to each other through reaction kinetics, they were globally fit by minimizing the sum of reduced chi-square values at all positive time delays given by

$$\chi^2 = \frac{1}{N - m} \sum_{j=\text{time delay}} \sum_i \left(\frac{\Delta S_{\text{theory}}(q_i, t_j) - \Delta S_{\text{experimental}}(q_i, t_j)}{\sigma_{i,j}} \right)^2 \quad (2)$$

where N is the number of data points along the q axis, m is the number of fitting parameters, and $\sigma_{i,j}$ is the standard deviation of the scattering curve at a given time delay t_j . The reduced χ^2 is commonly used as a measure of the goodness of a fit and the value of 1 means the best fit. The minimization was performed in the q range from 0.5 to 8.5 Å⁻¹. The global-fitting parameters consist of rate constants of various reaction pathways, branching ratios among photoproducts, and the size of laser spot at the sample. The χ^2 was minimized using the MINUIT package written at CERN.³⁹

In the global fitting analysis, we fit the experimentally measured difference scattering curves using theoretical difference scattering curves. The model function for the theoretical difference scattering accounts for three major components contributing to the signal: (i) solute-only term, (ii) solute–solvent cross term (called the cage term), and (iii) solvent-only term, as in the following expression:

$$\begin{aligned} \Delta S(q,t) &= \Delta S_{\text{solute-only}}(q,t) + \Delta S_{\text{solute-solvent}}(q,t) + \Delta S_{\text{solvent-only}}(q,t) \\ &= \Delta S_{\text{solute-related}}(q,t) + \Delta S_{\text{solvent-only}}(q,t) \\ &= \frac{1}{R} \left[\sum_k c_k(t) S_k(q) - S_g(q) \sum_k c_k(0) \right] \\ &\quad + \left[\left(\frac{\partial S}{\partial T} \right)_\rho \Delta T(t) + \left(\frac{\partial S}{\partial \rho} \right)_T \Delta \rho(t) \right] \end{aligned} \quad (3)$$

where R is the ratio of the number of solvent molecules to that of solute molecules, k is the index of the solute species (reactants, intermediates and products), $c_k(t)$ is the concentration of k^{th} species as a function of time delay t , $S_k(q)$ is the solute-related (that is, solute-only and cage components) scattering intensity of k^{th} species, and $S_g(q)$ is the scattering intensity related to the reactants ($g = \text{reactants}$). $(\partial S(q)/\partial T)_\rho$ is the change in the solvent scattering intensity in response to the temperature rise at a constant density, $(\partial S(q)/\partial \rho)_T$ is the solvent scattering change with respect to the change of solvent density at a constant temperature, and $\Delta T(t)$ and $\Delta \rho(t)$ are the changes in temperature and density of the solvent, respectively, at a time delay t . The $S_k(q)$'s were calculated from the molecular structures obtained from DFT calculation and the atom–atom pair distribution functions, $g(r)$, obtained from MD simulation. The details of the DFT calculation and the MD simulation are described in the next sections. We performed the DFT calculation and MD simulation for all the possible intermediates and products (C₂H₄I₂, C₂H₄I, C₂H₄I–I, C₂H₄, I₂, and I) included in the kinetic scheme in Figure S1 in the Supporting Information (SI). The $g(r)$'s of all the chemical species considered in our analysis are shown in Figure S2 in the SI. The solvent differential functions, $(\partial S(q)/\partial T)_\rho$ and $(\partial S(q)/\partial \rho)_T$, that account for solvent heating and expansion were determined from a separate measurement where pure cyclohexane solvent is vibrationally excited by near-infrared light.⁴⁰

Table 1. Structural Parameters of the Chemical Species Considered in the Kinetic Scheme^a

structural parameters	optimized values
C ₂ H ₄ I ₂	
C ₁ –C ₂	1.51 Å
C ₁ –I ₁ ^b	2.15 Å
C ₂ –I ₁	3.02 Å
I ₁ –I ₂	5.02 Å
I ₁ –C ₁ –C ₂ ^b	110.15°
I ₁ –C ₁ –C ₂ –I ₂	180°
C ₂ H ₄ I bridge	
C–C	1.33 Å
C–I ^c	3.13 Å
I–C–C ^c	77.69°
C ₂ H ₄ I–I	
C–C	1.33 Å
C–I ₁	3.29 Å
C–I ₂	5.94 Å
I ₁ –I ₂	2.68 Å
I ₁ –C–C	78.37°
C ₂ H ₄	
C–C	1.32 Å
I ₂	
I–I	2.66 Å

^a These values were obtained from the structures optimized by DFT calculation. To better match the experimental curve for the contribution of C₂H₄I radical only, we modified the structures of C₂H₄I₂ and C₂H₄I by tuning the C–I distances and I–C–C angles. ^b To fit the contribution of only C₂H₄I radical shown in Figure 9, we modified these two parameters while keeping the I₁–I₂ distance unchanged. The optimum values for C₁–I₁ and I₁–C₁–C₂ were determined to be 2.25 Å and 101.49°, respectively. ^c To fit the contribution of only C₂H₄I radical shown in Figure 9, we modified these two parameters. The optimum values for C–I and I–C–C were determined to be 3.47 Å and 78.92°, respectively.

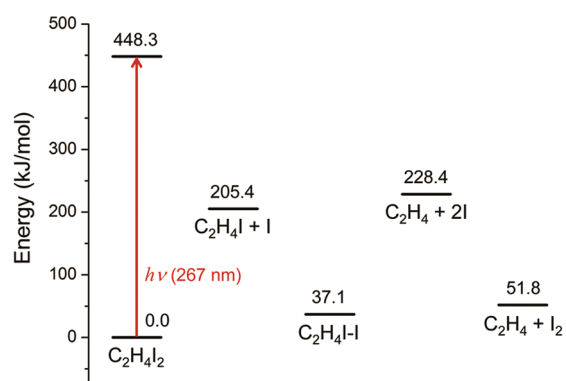


Figure 3. Energies of the chemical species involved in the iodine elimination reaction of C₂H₄I₂. The energy values were calculated by DFT method using ω B97X functional. The energies shown in the diagram were calculated relative to the energy of the C₂H₄I₂ parent molecule in the ground state.

Density Functional Theory Calculation. The structures of reactants and their presumed photoproducts were calculated using density functional theory (DFT) method. We used ω B97X

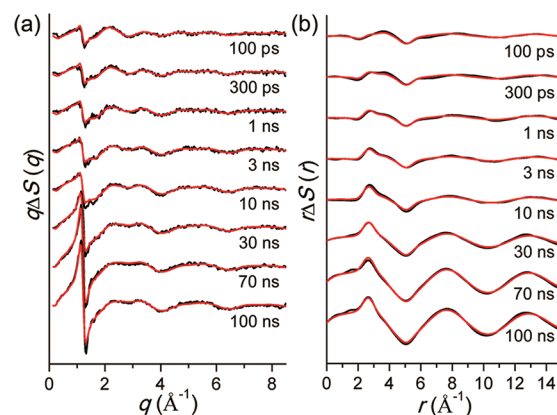


Figure 4. Difference scattering curves of C₂H₄I₂ in cyclohexane at various time delays after photolysis at 267 nm. (a) Experimental (black) difference scattering curves represented as $q\Delta S(q)$ in q -space and theoretical curves (red) obtained by global fitting analysis of the experimental data. (b) Difference RDFs, $r\Delta S(r)$, obtained by sine-Fourier transformation of the $q\Delta S(q)$ difference scattering curves shown in (a).

functional as DFT exchange-correlation functional, and all quantum chemical calculations were carried out by the Gaussian09 program.⁴¹ It was found that ω B97X is well suited for predicting the molecular structure of halomethane and haloethane, giving the bond lengths that agree well with experimental values or calculated values using high-level ab initio methods such as CCSD(T).⁴² As a basis set, aug-cc-pVTZ-PP small-core relativistic effective core potential (RECP) was used for iodine so that the scalar relativistic effect of heavy element can be considered. We also used aug-cc-pVTZ all-electron basis sets for other atoms. To describe the solvent environment, the integral-equation-formalism polarizable continuum model (IEFPCM) method was used. The structures were fully optimized in the solvent environment and subsequent harmonic vibrational frequencies were calculated for the optimized structures. The structural parameters of the optimized structures are listed in Table 1. Also, based on the calculated energies of each species, a diagram containing the energies of all the reaction pathways considered in this work is shown in Figure 3.

Molecular Dynamics Simulation. The molecular dynamics (MD) simulations were done using the program MOLLY,⁴³ which has successfully simulated the molecules in the solution phase in previous works.^{4,7,10} The simulated solution system consists of one solute molecule surrounded by 256 cyclohexane molecules in a cubic box of ~ 26 Å. All simulations were performed at an ambient temperature (300 K) with a solvent density of 0.779 g/cm³. The system was equilibrated over 200 ps at a constant temperature via coupling to a Nose-Hoover thermostat.⁴⁴ The simulations were performed in the NVT ensemble with 1 fs time step and the trajectories were followed up to 1 ns. From the simulation, we obtained the atom–atom pair distribution functions, $g(r)$, from which the scattering intensity of each molecular species was calculated using our homemade codes and tabulated atomic form factors.

3. RESULTS AND DISCUSSION

Time-Resolved Difference Scattering of C₂H₄I₂ Photodissociation. The experimental difference scattering curves at various time delay points are shown in Figure 4a. The experimental

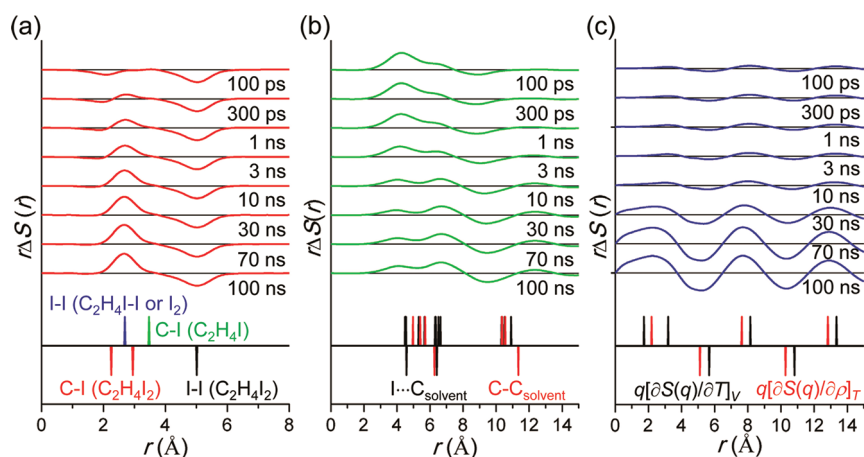


Figure 5. Difference RDFs represented in r -space are decomposed into three components: (a) the solute-only term, (b) the solute–solvent cross term (cage term), and (c) the solvent-only term. At the bottom of each plot, major features in the difference scattering curves are assigned by lines, which were obtained from the radial pair distribution functions, $g(r)$, calculated by the MD simulation. The lines in (a) correspond to the bond lengths of solute species calculated by DFT calculation. The black, red, green and blue lines correspond to $I-I$ of $C_2H_4I_2$, $C-I$ of $C_2H_4I_2$, $C-I$ of C_2H_4I radical, and $I-I$ of C_2H_4I-I or I_2 , respectively. The lines in (b) indicate the peak positions of broad $g(r)$ distributions for the $I \cdots C_{\text{solvent}}$ (black) and $C \cdots C_{\text{solvent}}$ (red) solute–solvent atomic pairs shown in Figure S2. In (a) and (b), the lines above the baseline correspond to the features related to the intermediates and products, while the lines below the baseline correspond to the features associated with the parent $C_2H_4I_2$ molecule. The lines in (c) indicate the features arising from the change in solvent temperature described by $q[\partial S(q)/\partial T]_V$ (black) and the ones resulting from thermal expansion described by $q[\partial S(q)/\partial \rho]_T$ (red). All the solvent features arise from the $C \cdots C$ atomic pairs in cyclohexane.

difference scattering curves were obtained by the difference between the signal measured at a positive time delay and the reference signal measured at the time delay of -3 ns, which corresponds to the scattering signal of the unexcited sample. The difference scattering curves show distinct oscillatory features, which are the signature of structural changes of reacting molecules. The best-fit theoretical difference scattering curves obtained from the global fitting analysis described in the Experimental Section are shown together with the experimental curves in Figure 4a. The difference scattering curve in q -space, $q\Delta S(q)$, can be sine-Fourier transformed into real space, giving the difference radial distribution functions (RDFs), $r\Delta S(r)$, where r is the interatomic distance (Figure 4b). Because the difference RDF represents the change of interatomic distances of the chemical species participating in the reaction, it serves as an intuitive measure of the structural change of the reacting molecules.

However, because the solution scattering signal is a mixture of solute, cage, and solvent terms, the features in the raw difference RDFs are very broad and it is difficult to clearly assign them to specific atom–atom pairs of the chemical species. To assign the features in the difference scattering curves more clearly, we decomposed the difference RDFs shown in Figure 4b into three components: the solute term, the solute–solvent cross term (cage term), and the solvent term, as shown in Figure 5. We assigned the major features of the difference scattering using the lines drawn at the bottom of each plot in Figure 5. These lines were obtained from the atom–atom pair distribution functions, $g(r)$, calculated from the MD simulation implemented for all the chemical species involved in the reaction. The $g(r)$ represents the distribution of distance between an atom–atom pair, and the theoretical scattering curve of each species was calculated from the $g(r)$ as well. The $g(r)$'s of all the chemical species used in our analysis are shown in Figure S2 in the SI. Because each line in Figure 5 has different degrees of broadening and contribution to the total difference RDF signal, individual lines might not exactly match the positions of the peaks in the difference RDFs.

The solute-only term shown in Figure 5a clearly demonstrates the structural evolution of the reacting solute molecules. For example, at 100 ps, two negative peaks are distinct at 2.1 and 5.0 Å and mainly reflect the distances of $C-I$ and $I-I$ atomic pairs, respectively, of depleted $C_2H_4I_2$ (anti) parent molecule. As the reaction progresses, a positive peak at 2.7 Å grows up. This peak corresponds to the $I-I$ atomic pair of C_2H_4I-I isomer or I_2 and indicates the formation of the two species. Besides these peaks, a negative contribution from the $C-I$ distance (3.0 Å) of the $C_2H_4I_2$ molecule and a positive contribution from the $C-I$ distance (3.5 Å) of the C_2H_4I radical are present but are hidden by other features of larger amplitude and broadening.

From the solute–solvent cross-term in Figure 5b, the information on the solvent environment around the solutes can be obtained. At 100 ps, two positive peaks centered at 4.2 and 6.4 Å and a negative peak at 8.9 Å are distinct. The appearance of positive peaks at smaller distances than the negative peak indicates that the average distance between the solute and solvent molecules decreases due to fragmentation of the parent molecule into smaller species. As a result, one cage splits to many cages of smaller sizes. As the reaction progresses, the positions and amplitudes of the peaks keep changing, giving two positive peaks at 3.8 and 6.8 Å and a negative peak at 9.5 Å at 100 ns with modified peak amplitudes. This change in the difference scattering pattern reflects the dynamic rearrangement of the solvent cage structure in response to the formation and dissociation of the transient solute species.

From the solvent-only term in Figure 5c, one can obtain the information on heat dissipation and subsequent solvent rearrangement induced by photoexcitation and photoreaction. The difference scattering of the solvent consists of $q[\partial S(q)/\partial T]_V$ and $q[\partial S(q)/\partial \rho]_T$ terms. The $q[\partial S(q)/\partial T]_V$ term is responsible for the increase in temperature (and pressure) of the solvent at a constant volume, which occurs at early stage of the reaction (<10 ns). The $q[\partial S(q)/\partial \rho]_T$ term accounts for the thermal expansion that occurs after 10 ns. The expansion leads to the

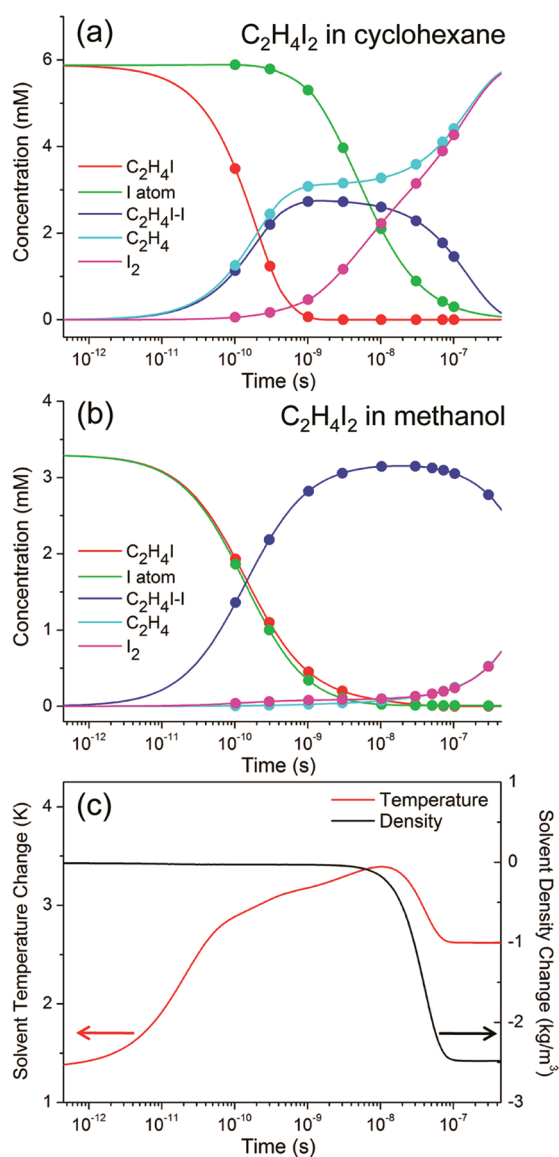


Figure 6. (a) Time-dependent concentration changes of chemical species involved in the photodissociation reaction of C₂H₄I₂ in cyclohexane obtained from global fitting analysis. C₂H₄I radical (red), I atom (green), C₂H₄I-I isomer (blue), C₂H₄ (cyan), and I₂ (magenta). The dots indicate the time points where we have the scattering data. (b) The concentration changes of the same reaction in methanol adapted from ref 4. The color codes are the same as in (a). (c) Time-dependent changes of solvent temperature (red) and density (black) induced by photodissociation of C₂H₄I₂. Before 10 ns, the heat dissipated from the photoreaction induces the temperature increase at a constant volume. After 10 ns, the thermal expansion occurs and the density of the solvent decreases with ~ 30 ns time constant.

equilibration with an ambient pressure and the decrease of the solvent density. As a result, the C \cdots C distances in adjacent cyclohexane molecules change, resulting in highly oscillatory features in the difference scattering curves after 10 ns.

Kinetics and Mechanism of C₂H₄I₂ Photodissociation. Figure 6a shows time-dependent concentration changes of chemical species obtained from the global fitting analysis. For comparison, the concentration kinetics of the same reaction in methanol were adapted from the previous TRXL study⁴ and

shown in Figure 6b. Both in cyclohexane and methanol, after photoexcitation, one iodine atom is dissociated from C₂H₄I₂ molecule and C₂H₄I radical is formed much earlier than 100 ps. However, subsequent reaction pathways starting from C₂H₄I radical are quite different between the two solvents. In methanol, the C₂H₄I radical combines with I atom to form C₂H₄I-I isomer, which then dissociates into C₂H₄ and I₂ molecule. In contrast, in cyclohexane, the C₂H₄I radical undergoes two competing reaction channels: (1) reacts with I atom to form C₂H₄I-I isomer or (2) further dissociates into C₂H₄ and I.

The channel 1, C₂H₄I + I \rightarrow C₂H₄I-I (isomer formation), in cyclohexane occurs with a bimolecular time constant of $4.17 (\pm 0.04) \times 10^{11} \text{ M}^{-1} \text{ s}^{-1}$, which is larger by 1 order of magnitude than the rate constant for nongeminate recombination of molecular iodine in *n*-hexane solvent.⁴⁵ The faster formation of the isomer than molecular iodine suggests that the isomer is formed via in-cage geminate recombination. This rate constant is about half of the value determined in methanol ($7.94 \times 10^{11} \text{ M}^{-1} \text{ s}^{-1}$), suggesting that the isomer is formed more slowly in cyclohexane than in methanol. The isomer eventually dissociates into the final products of C₂H₄ and I₂ with a rate constant of $6.31 (+11.89/-4.12) \times 10^6 \text{ s}^{-1}$, which is larger by 1 order of magnitude than in methanol ($1.99 \times 10^5 \text{ s}^{-1}$), suggesting a shorter lifetime of C₂H₄I-I isomer in cyclohexane than in methanol.

The channel 2, C₂H₄I \rightarrow C₂H₄ + I (direct dissociation), occurs with a rate constant of $2.69 (\pm 0.01) \times 10^9 \text{ s}^{-1}$. Considering that the isomer formation is a bimolecular process and the concentration of iodine atom is 5.9 mM when the reaction channel 1 starts to occur, both channels 1 and 2 occur on very similar time scales with ~ 400 ps time constant. As a result, the two channels are equally branched to form similar concentrations of C₂H₄I-I and C₂H₄ (48:52) at ~ 1 ns, when both reaction channels 1 and 2 are completed. Following the occurrence of channel 2, the I atoms nongeminately recombine with each other to form molecular iodine in tens of ns with a bimolecular rate constant of $1.58 (\pm 0.10) \times 10^{10} \text{ M}^{-1} \text{ s}^{-1}$, which is comparable to the rate constant for nongeminate recombination determined in *n*-hexane ($1.8 \times 10^{10} \text{ M}^{-1} \text{ s}^{-1}$).⁴⁵ As a result of the significant contribution from channel 2, the concentration changes of C₂H₄ and I₂ exhibit more complex, multiexponential dynamics compared to the same reaction in methanol, as shown in Figure 6a,b. The rate constants and branching ratios for all the reaction pathways are summarized in Table 2. For comparison, the parameters obtained from the global fitting of the data in methanol were excerpted from the earlier work^{4,40} and listed together in Table 2.

Besides the concentration dynamics of the solute species, we can also obtain the information on the dynamics of solvent heating and expansion. When the reactant molecules are photoexcited by laser pulses, a fraction of molecules (36% in our result) rapidly recover back to the ground state by geminate recombination and vibrational cooling in the ground state, thus dissipating the heat to the environment. As a result, the temperature and density of the solvent in the laser focal volume are affected, as shown in Figure 6c. At early time delays until 10 ns, the heat is dissipated at a constant volume, leading to the increase of temperature by a total of 3.4 K at 10 ns, as described by the solvent differential of $q(\partial S(q)/\partial T)_p$. After 10 ns, thermal expansion occurs and thus the solvent density decreases with ~ 30 ns time constant, giving a total change of -2.5 kg/m^3 at 100 ns. With the expansion, the solvent temperature also decreases, giving a total temperature change of 2.6 K at 100 ns. Although the heat capacities of cyclohexane ($C_v = 113.64 \text{ J} \cdot \text{mol}^{-1} \text{ K}^{-1}$,

Table 2. Fitting Parameters Obtained from Global Fitting Analysis of C₂H₄I₂ in Cyclohexane

	cyclohexane	methanol ^a
fraction of photoexcited molecules	0.15 (±0.001) ^b	0.16
fraction of rapidly cooled molecules	0.36 (±0.005) ^c	0.65
C ₂ H ₄ I ₂ → C ₂ H ₄ I + I ^d	1.00 × 10 ¹⁴ s ⁻¹	1.00 × 10 ¹⁴ s ⁻¹
C ₂ H ₄ I ₂ → C ₂ H ₄ + I ₂ ^e	0.0	0.0
C ₂ H ₄ I ₂ → C ₂ H ₄ + 2I ^e	0.0	0.0
C ₂ H ₄ I + I → C ₂ H ₄ I–I	4.17 (±0.04) × 10 ¹¹ M ⁻¹ s ⁻¹	7.94 × 10 ¹¹ M ⁻¹ s ⁻¹
C ₂ H ₄ I → C ₂ H ₄ + I	2.69 (±0.01) × 10 ⁹ s ⁻¹	2.00 × 10 ⁷ s ⁻¹
C ₂ H ₄ I–I → C ₂ H ₄ + I ₂ ^f	6.31 (+11.89/–4.12) × 10 ⁶ s ⁻¹	1.99 × 10 ⁵ s ⁻¹
I + I → I ₂	1.58 (±0.10) × 10 ¹⁰ M ⁻¹ s ⁻¹	3.16 × 10 ¹⁰ M ⁻¹ s ⁻¹
laser spot radius (μm)	48 (±0.66)	51
temperature change at 100 ns (K)	2.6	2.1
density change at 100 ns (kg/m ³)	–2.5	–2.5

^aThe optimized parameters for the reaction in methanol were excerpted from the previous TRXL work.⁴⁰ ^bThis value is the fraction of concentration of photoexcited molecules vs the concentration of the C₂H₄I₂ solution (60 mM) in the ground state. ^cThis value is the fraction of rapidly cooled molecules with respect to the photoexcited molecules. Therefore, the concentration of molecules that undergoes photodissociation is calculated by (concentration of the C₂H₄I₂ solution in the ground state) × (concentration of photoexcited molecules) × (1 – fraction of rapidly cooled molecules). ^dThis parameter was fixed at this value. Because this process is faster than the time resolution of 100 ps, the global fitting was not affected by this parameter. ^eThis parameter was fixed at this value because they converged to very small values. Because this process is much slower than the time range of our experimental data (up to 100 ns), it did not affect the global fitting. ^fThis parameter exhibits a large error because this process is at the border of time range of our experimental data (up to 100 ns) and have much uncertainty.

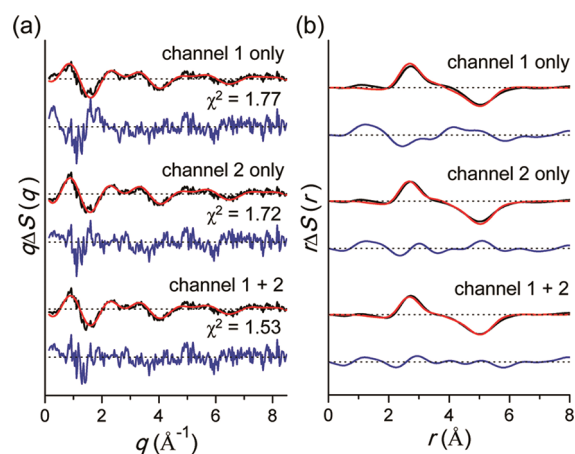


Figure 7. Comparison of the global fitting using the models employing only channel 1 (top, isomer formation), only channel 2 (middle, direct dissociation of C₂H₄I radical), or both channels (bottom) in (a) *q*-space and (b) *r*-space. The solute-only term was carefully extracted from the data at 3 ns, where both C₂H₄I–I and C₂H₄ are abundant in cyclohexane. At the same time delay, only the C₂H₄I–I isomer was a dominant species in methanol. The experimental (black) and theoretical (red) scattering curves of the solute-only term are shown together with the residual (blue) obtained by their difference multiplied by a factor of 3. The reduced chi-square value for each fit is shown above the residual. It can be seen that the best fit is obtained from the model using both channels.

$C_p = 156.0 \text{ J} \cdot \text{mol}^{-1} \text{ K}^{-1}$) are much higher than those of methanol ($C_v = 69.5 \text{ J} \cdot \text{mol}^{-1} \text{ K}^{-1}$, $C_p = 81.1 \text{ J} \cdot \text{mol}^{-1} \text{ K}^{-1}$), the change in the temperature and density of the solvent is equivalent in cyclohexane and methanol (see Table 2). This observation is accounted for by a smaller fraction of molecules that are rapidly cooled back to the ground state in cyclohexane than in methanol.

Solvent Dependence of Reaction Dynamics. We obtained the kinetics and mechanism from the analysis of the data measured in cyclohexane. As discussed earlier, we are to examine

the effect of solvent on the reaction dynamics by comparing with the TRXL result measured in methanol. The cyclohexane and methanol have very different polarity, and the solvent polarity is known to significantly affect the rates and pathways of a chemical reaction. For example, photodissociation of diiodomethane (CH₂I₂) was studied in both methanol and cyclohexane using the same TRXL approach.^{5,46} From those studies, it was revealed that the fate of the iodine radicals is determined by the polarity of the solvent, that is, I₃⁻ is formed in polar methanol and I₂ is formed in nonpolar cyclohexane. In addition, the lifetime and I–I distance of the CH₂I–I isomer were determined to be much different in polar methanol and in nonpolar cyclohexane.

From a comparison of the reaction kinetics in cyclohexane and methanol solvents, we note that the biggest differences are that (1) the reaction pathway from C₂H₄I radical is branched into two channels only in cyclohexane and (2) the C₂H₄I–I isomer lives much shorter in cyclohexane than in methanol. First of all, to validate the branching into the two reaction channels from C₂H₄I radical, we performed the global fitting analysis by including only one of the two channels. To do so, we fixed the rate constant for either channel 1 or channel 2 at zero. To compare the models employing only channels 1 or 2 with the model using both channels, we carefully extracted the solute-only term from the 3 ns data, where both C₂H₄I–I isomer and C₂H₄ product are abundant in cyclohexane as shown in Figure 6a. At the same time delay, only C₂H₄I–I isomer was a dominant species in methanol, as can be seen in Figure 6b. When comparing the solute-only terms obtained from global fitting using the three models as shown in Figure 7, the model using both channels gives a better fit with a smaller reduced chi-square value than the one using only channel 1 or channel 2. Also, the sums of reduced chi-square values for all the data at eight time delays are 13.7 and 14.4 for the model using only channel 1 or channel 2, respectively. These values are significantly larger than the sum of reduced chi-square values (12.7) from the model using both channels, confirming that both reaction channels occur in cyclohexane.

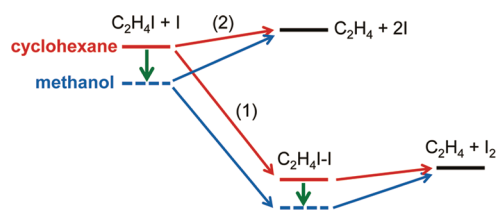


Figure 8. Energy diagram for the reaction channels starting from C_2H_4I radical. Because the C_2H_4I radical ($\mu = 2.0$ D) is more stable in methanol than in cyclohexane, the endothermic reaction channel (2) is easier to occur in cyclohexane. In contrast, the C_2H_4I-I isomer ($\mu = 1.6$ D) is also more stable in methanol than in cyclohexane, and therefore, the highly exothermic channel (1) is less likely to be affected by the change in solvent polarity. Meanwhile, due to the stabilization of the C_2H_4I-I isomer in methanol, the dissociation of C_2H_4I-I into C_2H_4 and I_2 is easier to occur in cyclohexane than in methanol, leading to a shorter lifetime of the isomer.

The two differences between the reactions in cyclohexane and in methanol can be explained in terms of the solvent polarity. As can be seen in the energy diagram in Figure 3, the channel 1 ($C_2H_4I + I \rightarrow C_2H_4I-I$) is highly exothermic, while the channel 2 ($C_2H_4I \rightarrow C_2H_4 + I$) is slightly endothermic. Because C_2H_4 and I (products of the channel 2) are nonpolar and the C_2H_4I radical (reactant of both channel 1 and channel 2) is polar ($\mu = 2.0$ D), only the C_2H_4I radical is more stable in methanol than in cyclohexane (see Figure 8). As a result, the endothermic channel 2 is easier to occur in cyclohexane than in methanol. In contrast, the C_2H_4I-I isomer (product of channel 1) is also highly polar ($\mu = 1.6$ D) and more stable in methanol than in cyclohexane (but to a lesser degree than C_2H_4I radical), and therefore, the highly exothermic channel 1 is less likely to be influenced by the change in solvent polarity. Thus, channel 1 occurs in both methanol and cyclohexane, while channel 2 is more likely to occur in nonpolar cyclohexane than in polar methanol. The shorter lifetime of the C_2H_4I-I isomer can be also ascribed to the polarity of the solvent. As can be seen in Figure 3, $C_2H_4I-I \rightarrow C_2H_4 + I_2$ is an endothermic reaction. As mentioned above, C_2H_4I-I isomer (reactant of $C_2H_4I-I \rightarrow C_2H_4 + I_2$) is more stable in methanol than in cyclohexane. In contrast, C_2H_4 and I_2 (products of $C_2H_4I-I \rightarrow C_2H_4 + I_2$) have zero dipole moments and will be less affected by the polarity of the solvent. Therefore, dissociation of the C_2H_4I-I isomer is easier to occur in cyclohexane than in methanol, leading to a shorter lifetime of the isomer in cyclohexane. In summary, the emergence of the channel 2 ($C_2H_4I \rightarrow C_2H_4 + I$) and the shorter lifetime of C_2H_4I-I isomer in cyclohexane compared to the same reaction in methanol are the evidence for the role of the solvent in the chemical reaction. In other words, the solvent changes the landscape of the potential energy surfaces and thus alters the reaction pathways of a chemical reaction.

Determination of Radical Structure. As discussed above, the structure of haloethyl radical has been controversial between the classical and bridged forms. Only recently, the TRXL study of $C_2H_4I_2$ photodissociation in methanol⁴ directly revealed that the C_2H_4I radical has the bridged structure. To examine if the radical structure is influenced by the polarity of the solvent, we performed the global fitting by including only either bridged or anti structure of C_2H_4I radical in the fitting. As a quantitative measure of fitting quality between the two models, we calculated the ratio of reduced chi-square values between the bridged and anti model at each time delay from the best-fit result of each model. As can

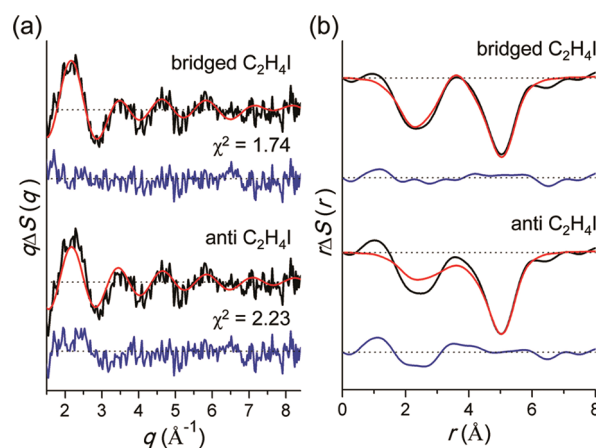


Figure 9. Comparison of models using only either bridged or classical (anti) structure of C_2H_4I radical. The contribution only associated with the formation of C_2H_4I radical ($C_2H_4I_2 \rightarrow C_2H_4I + I$) were extracted from the experimental data at 100 ps (and its theoretical fit) by subtracting the cage and solvent terms as well as the contribution of other solute species. The extracted experimental (black) and theoretical (red) scattering curves for the formation of C_2H_4I radical only are compared in the (a) q -space and (b) r -space. The blue curve represents the residual obtained by subtracting the theoretical curve from the experimental curve. The reduced chi-square value for each fit is shown above the residual. The bridged structure gives a much better fit than the anti structure. In fact, when including both bridged and anti radicals in the fitting with their concentration ratio as a variable, the concentration of the anti radical converges to zero.

be seen in Figure S3 in the SI, the $\chi^2_{\text{bridge}}/\chi^2_{\text{anti}}$ ratio is significantly lower than 1 at 100 ps, where the concentration of the C_2H_4I radical is high. As the concentration of C_2H_4I radical decreases at later time delays, the ratio expectedly approaches 1. Therefore, the bridged radical gives a better fit to the experimental data than the anti radical. In fact, when we include a mixture of bridged and anti structures in the fitting with their concentration ratio as a variable, the concentration of the anti radical converges to zero.

To have better structural distinction between the two radical structures, we carefully extracted only the contribution related to the $C_2H_4I_2 \rightarrow C_2H_4I + I$ pathway. To do so, we subtracted the contributions of solvent, cage, and other solute species from the data at 100 ps. The extracted contributions of only C_2H_4I radical for the bridged and anti models are shown in Figure 9. The negative peak at 5 Å corresponds to I-I distance of the depleted parent molecule and is common for both models. However, we can see that the shapes of the peak in the r -range of 1–4 Å are quite different between the two models. This region corresponds to the distances of I atom relative to two carbon atoms in the radical. Because the bridged structure has only one C-I distance due to its symmetric geometry and the anti structure has two C-I distances, the difference of the peak shape in this region serve as a clear signature of the bridged structure. Considering that the bridged model fits the experimental data at 100 ps much better than the anti model, it is clear that the bridged model gives a much better fit to the experimental data than the anti model.

We note that, when we use the structures of C_2H_4I bridged radical and $C_2H_4I_2$ parent molecule calculated from the DFT calculation as they are (as listed in Table 1), the fit is not as good as shown in Figure 9. This observation suggests that the calculated structure might not correctly reproduce the transient struc-

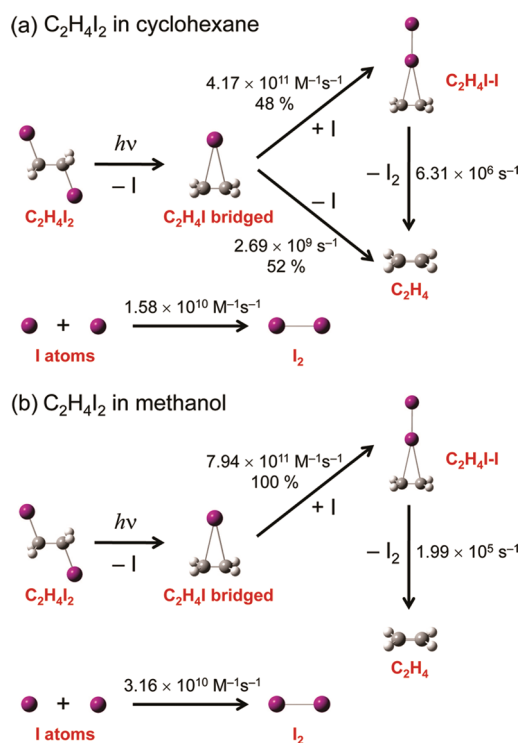


Figure 10. Schematic of the reaction mechanisms (a) in cyclohexane and (b) in methanol determined by the TRXL measurement and global fitting analysis. The rate constants and branching ratios are shown for each reaction pathway.

ture generated in the experiment. To correct for the difference in the structure, we fine-tuned the structures of both C_2H_4I bridged radical and $C_2H_4I_2$ molecule by varying the C–I distances and C–C–I angles so that the theoretical and experimental curves from only C_2H_4I radical are best matched. From the structure optimization, the best fit is obtained when the C–I distances of C_2H_4I bridged radical and $C_2H_4I_2$ molecule are elongated by 0.34 Å (C–I = 3.47 Å) and 0.10 Å (C₁–I₁ = 2.25 Å), respectively (For details, see Table 1). By using these modified structures of C_2H_4I bridged radical and $C_2H_4I_2$ molecule in the global fitting, the overall fitting quality for all the data at various time delays significantly improved as well. This result underpins the sensitivity of TRXL technique to molecular structure.

4. CONCLUSION

In this work, we investigated the kinetics and mechanism of the elimination reaction of $C_2H_4I_2$ in cyclohexane. By analyzing the time-resolved X-ray scattering patterns measured from the solution sample, we extracted the detailed structural changes of intermediate and product species and their kinetics. In particular, the global structural sensitivity of the TRXL allowed us to detect the branching of the reaction pathways from C_2H_4I radical and to directly identify the structure of C_2H_4I radical. Compared with an earlier work on the same reaction using the same TRXL experimental approach but implemented in polar methanol solvent, the reaction in cyclohexane exhibit quite different reaction dynamics and mechanism. The solvent dependence can be explained by the difference in the polarity of solvents. We summarized the reaction mechanism, kinetic rates, and the

radical structure of $C_2H_4I_2$ photodissociation in both cyclohexane and methanol in Figure 10.

■ ASSOCIATED CONTENT

S Supporting Information. Supplemental Figures S1–3. This material is available free of charge via the Internet at <http://pubs.acs.org>.

■ AUTHOR INFORMATION

Corresponding Author

*E-mail: hyotcherl.ihee@kaist.ac.kr

■ ACKNOWLEDGMENT

This work was supported by the Creative Research Initiatives (Center for Time-Resolved Diffraction) of MEST/NRF. J.H.L., S.J., K.H.K., and T.W.K. acknowledge the support from the WCU program (R31-2008-000-10071-0).

■ REFERENCES

- Ihee, H. *Acc. Chem. Res.* **2009**, *42*, 356.
- Kim, T. K.; Lee, J. H.; Wulff, M.; Kong, Q.; Ihee, H. *Chem-PhysChem* **2009**, *10*, 1958.
- Ihee, H.; Wulff, M.; Kim, J.; Adachi, S. *Int. Rev. Phys. Chem.* **2010**, *29*, 453.
- Ihee, H.; Lorenc, M.; Kim, T. K.; Kong, Q. Y.; Cammarata, M.; Lee, J. H.; Bratos, S.; Wulff, M. *Science* **2005**, *309*, 1223.
- Davidsson, J.; Poulsen, J.; Cammarata, M.; Georgiou, P.; Wouts, R.; Katona, G.; Jacobson, F.; Plech, A.; Wulff, M.; Nyman, G.; Neutze, R. *Phys. Rev. Lett.* **2005**, *94*, 245503.
- Plech, A.; Kotaidis, V.; Lorenc, M.; Boneberg, J. *Nat. Phys.* **2006**, *2*, 44.
- Kim, T. K.; Lorenc, M.; Lee, J. H.; Lo Russo, M.; Kim, J.; Cammarata, M.; Kong, Q.; Noel, S.; Plech, A.; Wulff, M.; Ihee, H. *Proc. Natl. Acad. Sci. U.S.A.* **2006**, *103*, 9410.
- Georgiou, P.; Vincent, J.; Andersson, M.; Wohri, A. B.; Gourdon, P.; Poulsen, J.; Davidsson, J.; Neutze, R. *J. Chem. Phys.* **2006**, *124*, 234507.
- Kotaidis, V.; Dahmen, C.; von Plessen, G.; Springer, F.; Plech, A. *J. Chem. Phys.* **2006**, *124*, 184702.
- Lee, J. H.; Kim, J.; Cammarata, M.; Kong, Q.; Kim, K. H.; Choi, J.; Kim, T. K.; Wulff, M.; Ihee, H. *Angew. Chem., Int. Ed.* **2008**, *47*, 1047.
- Lee, J. H.; Kim, T. K.; Kim, J.; Kong, Q.; Cammarata, M.; Lorenc, M.; Wulff, M.; Ihee, H. *J. Am. Chem. Soc.* **2008**, *130*, 5834.
- Plech, A.; Kotaidis, V.; Siems, A.; Sztucki, M. *Phys. Chem. Chem. Phys.* **2008**, *10*, 3888.
- Haldrup, K.; Christensen, M.; Cammarata, M.; Kong, Q.; Wulff, M.; Mariager, S. O.; Bechgaard, K.; Feidenhans'l, R.; Harrit, N.; Nielsen, M. M. *Angew. Chem., Int. Ed.* **2009**, *48*, 4180.
- Christensen, M.; Haldrup, K.; Bechgaard, K.; Feidenhans'l, R.; Kong, Q. Y.; Cammarata, M.; Lo Russo, M.; Wulff, M.; Harrit, N.; Nielsen, M. M. *J. Am. Chem. Soc.* **2009**, *131*, 502.
- Kim, K. H.; Oang, K. Y.; Kim, J.; Lee, J. H.; Kim, Y.; Ihee, H. *Chem. Commun.* **2011**, *47*, 289.
- Kim, J.; Kim, K. H.; Kim, J. G.; Kim, T. W.; Kim, Y.; Ihee, H. *J. Phys. Chem. Lett.* **2011**, *2*, 350.
- Hynes, J. T. In *Ultrafast Dynamics of Chemical Systems*; Simon, J. D., Ed.; Kluwer Academic Publishers: Dordrecht, Netherlands, 1994; p 345.
- Bagchi, B.; Chandra, A. Collective orientational relaxation in dense polar liquids. In *Adv. Chem. Phys.*; Prigogine, I., Rice, S. A., Eds.; Wiley: New York, 1991; Vol. 80; p 1.
- Weaver, M. J. *Chem. Rev.* **1992**, *92*, 463.
- Free Radicals*; Kochi, J. K., Ed.; John Wiley & Sons: New York, 1973; Vol. II.

- (21) Beckwith, A. L. J.; Ingold, K. U. Free-Radical Rearrangements. In *Rearrangements in Ground and Excited States*; Mayo, P. d., Ed.; Academic Press: New York, 1980.
- (22) *Free Radicals in Organic Chemistry*; Fossey, J., Lefort, D., Sorba, J., Eds.; John Wiley & Sons: New York, 1995.
- (23) Goering, H. L.; Abell, P. I.; Aycocock, B. F. *J. Am. Chem. Soc.* **1952**, *74*, 3588.
- (24) Thaler, W. *J. Am. Chem. Soc.* **1963**, *85*, 2607.
- (25) Skell, P. S.; Tuleen, D. L.; Readio, P. D. *J. Am. Chem. Soc.* **1963**, *85*, 2849.
- (26) Skell, P. S.; Shea, K. J. Bridged Free Radicals. In *Free Radicals*; Kochi, J. K., Ed.; John Wiley & Sons: New York, London, Sydney, Toronto, 1973.
- (27) Engels, B.; Peyerimhoff, S. D. *J. Mol. Struct.* **1986**, *138*, 59.
- (28) Bernardi, F.; Fossey, J. *J. Mol. Struct.* **1988**, *180*, 79.
- (29) Ihee, H.; Zewail, A. H.; Goddard, W. A., III. *J. Phys. Chem. A* **1999**, *103*, 6638.
- (30) Zheng, X.; Phillips, D. L. *J. Phys. Chem. A* **2000**, *104*, 1030.
- (31) Bowles, A. J.; Hudson, A.; Jackson, R. A. *Chem. Phys. Lett.* **1970**, *5*, 552.
- (32) Edge, D. J.; Kochi, J. K. *J. Am. Chem. Soc.* **1972**, *94*, 6485.
- (33) Paul Maj, S.; Symons, M. C. R.; Trousson, P. M. R. *Chem. Commun.* **1984**, 561.
- (34) Rasmusson, M.; Tarnovsky, A. N.; Pascher, T.; Sundstrom, V.; Akesson, E. *J. Phys. Chem. A* **2002**, *106*, 7090.
- (35) Khundkar, L. R.; Zewail, A. H. *J. Chem. Phys.* **1990**, *92*, 231.
- (36) Zhong, D.; Ahmad, S.; Zewail, A. H. *J. Am. Chem. Soc.* **1997**, *119*, 5978.
- (37) Cao, J. M.; Ihee, H.; Zewail, A. H. *Proc. Natl. Acad. Sci. U.S.A.* **1999**, *96*, 338.
- (38) Ihee, H.; Goodson, B. M.; Srinivasan, R.; Lobastov, V. A.; Zewail, A. H. *J. Phys. Chem. A* **2002**, *106*, 4087.
- (39) James, F.; Roos, M. *Comput. Phys. Commun.* **1975**, *10*, 343.
- (40) Cammarata, M.; Lorenc, M.; Kim, T. K.; Lee, J. H.; Kong, Q. Y.; Pontecorvo, E.; Lo Russo, M.; Schiro, G.; Cupane, A.; Wulff, M.; Ihee, H. *J. Chem. Phys.* **2006**, 124.
- (41) Frisch, M. J.; Trucks, G. W.; Schlegel, H. B.; Scuseria, G. E.; Robb, M. A.; Cheeseman, J. R.; Scalmani, G.; Barone, V.; Mennucci, B.; Petersson, G. A.; et al. *Gaussian 09*, Revision A.1; Gaussian, Inc.: Wallingford, CT, 2009.
- (42) Kim, J.; Kim, T. K.; Ihee, H. *J. Phys. Chem. A* **2011**, *115*, 1264.
- (43) Refson, K. *Comput. Phys. Commun.* **2000**, *126*, 310.
- (44) Hoover, W. G. *Phys. Rev. A* **1985**, *31*, 1695.
- (45) Aditya, S.; Willard, J. E. *J. Am. Chem. Soc.* **1957**, *79*, 2680.
- (46) Vincent, J.; Andersson, M.; Eklund, M.; Wöhri, A. B.; Odelius, M.; Malmerberg, E.; Kong, Q.; Wulff, M.; Neutze, R.; Davidsson, J. *J. Chem. Phys.* **2009**, *130*, 154502.